Journal of The Electrochemical Society, **155** (3) B270-B280 (2008)
0013-4651/2008/155(3)/B270/11/$23.00 © The Electrochemical Society

Simulation of Electrochemical Impedance Spectra of Solid Oxide Fuel Cells Using Transient Physical Models

Yixiang Shi,[a] Ningsheng Cai,[a,z] Chen Li,[a] Cheng Bao,[a] Eric Croiset,[b,*] Jiqin Qian,[c] Qiang Hu,[c] and Shaorong Wang[c,*]

[a]*Key Laboratory for Thermal Science and Power Engineering of Ministry of Education, Tsinghua University, Beijing 100084, China*
[b]*Department of Chemical Engineering, University of Waterloo, Waterloo, Ontario N2L 3G1, Canada*
[c]*Shanghai Institute of Ceramics, Chinese Academy of Sciences (SICCAS), Shanghai 200050, China*

A general electrochemical impedance spectroscopy (EIS) modeling approach by directly solving a one-dimensional transient model based on physical conservation laws was applied for simulating EIS spectra of an anode-supported solid oxide fuel cell (SOFC) button cell consisting of Ni–yttria-stabilized zirconia |Ni–scandia-stabilized zirconia (ScSZ)|ScSZ|lanthanum strontium manganate (LSM)–ScSZ multiple layers. The transient SOFC model has been solved for imposed sinusoidal voltage perturbations at different frequencies. The results have then been transformed into EIS spectra. Six parameters had to be tuned (three for the cathode and three for the anode) and have been estimated using data from a symmetric cathode cell and from a button cell. The experimental and simulated EIS spectra were in good agreement for a range of temperatures (750–850°C), of feed compositions (mixture of $H_2/H_2O/N_2$), and of oxidants (air and oxygen). This approach can help in interpreting EIS spectra, as illustrated by identifying the contribution of transport limitation.
 [DOI: 10.1149/1.2825146]

Manuscript submitted August 1, 2007; revised manuscript received November 9, 2007. Available electronically January 16, 2008.

Fuel cell electrochemical systems are usually complex and are governed by coupled physicochemical processes such as chemical and electrochemical reactions, charge transport, and mass transport.[1,2] Because polarization curves can only provide a general description of the cell performance, electrochemical impedance spectroscopy (EIS) has become widely used in fuel cell research and development because it involves a relatively simple electrical measurement that gives detailed information about the fuel cell system, from mass-transport properties, chemical reaction rates, and dielectric properties to defects, microstructure, compositional influences, etc.[3] In this dynamic technique, usually a voltage perturbation is applied to a system and the amplitude and phase shift of the resulting current response are measured. Measurements can be conducted over a wide range of frequencies, resulting in the construction of impedance spectra.[4]

Most of the experimental data from EIS measurements have been interpreted using the equivalent-circuit model for its convenience, and detailed system information could be obtained from fitting the experimental data to the parameters of the equivalent-circuit elements.[5] Although the approach is useful and quite powerful, it often has limitations such as:

1. The approach can lead to ambiguities in data interpretations because the equivalent circuits are seldom unique except for only the simplest circuits. An equivalent circuit involving several circuit elements could often be rearranged in various configurations while still yielding the same impedance.

2. Detailed physical and chemical processes in the system cannot be predicted by equivalent-circuit models. For instance, the effects of current distributions and concentration distributions cannot be taken into account when interpreting data from equivalent-circuit models.

3. The measured system could only be approximated by circuit elements when assuming linear response of the system. The impedance is supposed to be independent of the amplitude of the applied signals. However, the electrochemical system could be highly nonlinear, especially for sinusoidal perturbations with high amplitudes. It was suggested that nonlinear EIS (NLEIS) measurements have several potential advantages.[6] For example, NLEIS better isolates the nonlinearities of specific physical processes and may offer improved measurement resolution.

To investigate solid oxide fuel cell (SOFC) electrode reaction kinetics, Miterdorfer and Gauckler[7-9] used a state-space model (SSM), which is widely used in control theory for solving complex differential equations. Bieberle and Gauckler[5] studied in depth elementary electrochemical reactions in SOFC anode by both experimental and SSM approaches. To simulate the electrochemical impedance spectra, the models were solved directly through the SSM approach. Bessler[10] presented a computational method for simulating EIS spectra based on transient numerical simulations of the reaction system. The impedance was then calculated in the time domain from the simulated periodic response of the system, maintaining its full nonlinear response. This method has been further validated by detailed modeling studies on SOFC EIS spectra achieved from gas-transport processes.[11] Gewies et al.[12] also applied this method on Ni/yttria-stabilized zirconia (YSZ) cermet anodes. Zhu and Kee[13] developed a time-accurate model to analyze EIS spectra in anode-supported button cells with internal methane reforming. This model represented significant advantages regarding physical conservation laws, porous media transport within the electrode, and heterogeneous chemistry reactions mechanisms, all of those being solved in the time domain. However, the spatial variations of ion and electron transport throughout the electrode structures were not considered.

In this paper, a general approach for EIS spectra simulation is applied by solving a comprehensive set of coupled transient models based on physical conservation laws. This simulation approach is illustrated by considering a transient model of an anode-supported SOFC button cell consisting of Ni–YSZ|Ni–scandia-stabilized zirconia (ScSZ)|ScSZ|LSM–ScSZ multiple layers. The simulation results of the EIS spectra were then compared to the measured EIS spectra under various conditions to prove the validity of both the transient model and the EIS simulation approach.

Experimental

Testing cell.— The anode-supported SOFC button cell used in this study consisted of a Ni/YSZ anode support layer (680 μm), a Ni/ScSZ anode active interlayer (15 μm), a ScSZ thin-film electrolyte layer (20 μm), and a lanthanum strontium manganate (LSM)/ScSZ cathode layer (15 μm).[14,15] Except for the cathode layer, which had a diameter of 1.4 cm, all other layers had a diameter of 2.6 cm.

Commercial NiO (Inco Ltd., Canada) was used with 8 mol % powder (Tosoh, Japan) for preparing the support layer and with SaSZ ($Zr_{0.89}Sc_{0.1}Ce_{0.01}O_{2-x}$, Daiichi Kigenso Kagaku Kogyo, Japan) for the anode active layer. The ratio of the mixtures (NiO–YSZ

* Electrochemical Society Active Member.
z E-mail: cains@mail.tsinghua.edu.cn

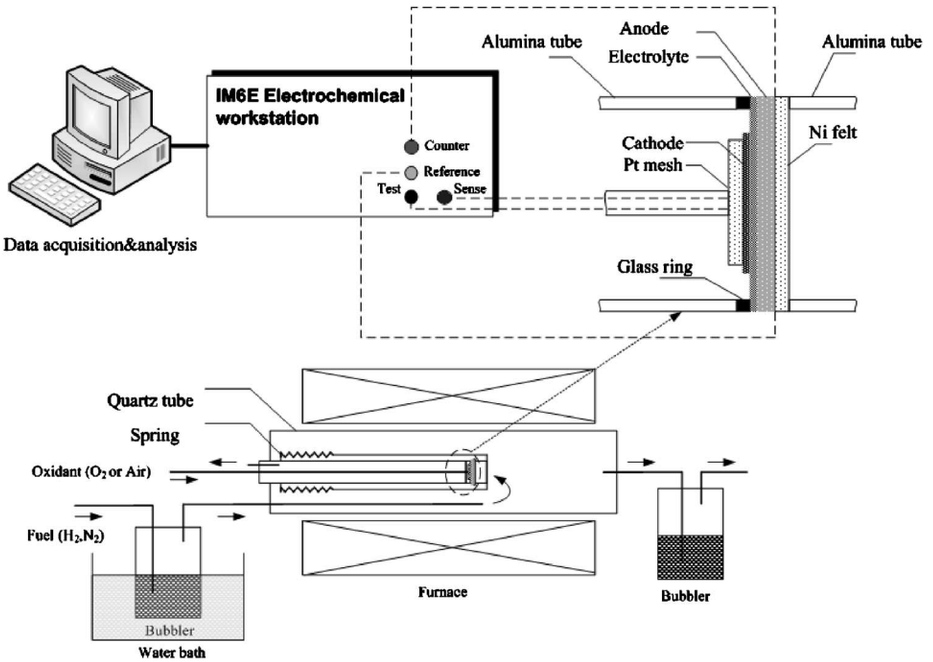

Figure 1. Schematic of the apparatus used to conduct EIS measurements.

and NiO–ScSZ) was 50 wt % NiO and 50 wt % stabilized zirconia. The ScSZ powder was also used to prepare the electrolyte film.

The slurries for the tape-casting process were prepared by a ball-milling process that included two steps. In the first step, all the above-mentioned ceramic powders were homogenized in a planetary mill for 2 h with dispersant in a mixture of methyl ethyl ketone and ethanol. To form sufficient porosity in the anode support and active layers, rice starch was added as a pore former to the mixture of NiO–YSZ and NiO–ScSZ with 40 wt % of each powders. Polyvinyl butyral and a mixture of polyethylene glycol and dibutyl *o*-phthalate were added as binder and plasticizer, respectively. The whole mixture was then milled for another 2 h.

Prior to tape casting, the slurries were vacuum pumped for about 2 min in order to remove the air. The ScSZ film was cast first onto the glass plate by a "doctor blade" method and allowed to dry in air for several minutes; the anode functional and active layers were prepared similarly. After drying overnight at room temperature, the multilayer green tape was detached and cosintered at 1400°C in air for 4 h.

The LSM (Inframat Advanced Materials, USA) and ScSZ powders in a mass ratio of 50:50 were mixed in a planetary mill with ethanol for 3 h to ensure random distribution of each phase. The dried mixture was subsequently ground in an agate mortar with ethyl cellulose and terpineol to prepare the paste, which was screen-printed onto the sintered ScSZ layer and sintered at 1200°C for 3 h to form the cathode.

Test setup and EIS measurement apparatus.— Figure 1 shows the in-house-built SOFC test station used for EIS measurement. The cell was located between two alumina tubes. Pt wires were used as voltage and current probe. A Pt mesh was used as cathode current collector and was fixed to the porous cathode with platinum paste. A porous Ni felt, which has a diameter of 1.4 cm and a thickness of 1.7 mm, was used as anode current collector and was fixed to the anode support layer with platinum paste. Before testing, the anode was fully reduced at 850°C in a $H_2/N_2/H_2O$ mixture. During the reduction step, the H_2 and N_2 flow rates were set at 10 and 40 sccm, respectively. H_2 or H_2–N_2 mixtures humidified at room temperature (30°C, i.e., 4% H_2O) were used as fuel, and oxygen or air was used as oxidant. The flow rate of fuel and oxidant were both kept at 50 sccm.

The EIS spectra were observed with a four-probe technique using an Electrochemical Workstation (IM6e, Zahner-Elektrik GmbH, Germany) over a temperature range of 700 to 850°C with an amplitude of 10 mV over a frequency range of 0.1 Hz to 100 kHz. The tests performed for model calibration and validation involved varying certain cell operating conditions. The following tests were carried out: (*i*) variable cell temperature 750, 800, and 850°C), (*ii*) variable oxidant (oxygen and air), and (*iii*) variable N_2 dilution (N_2 content in the dry fuel mixture: 0, 20, 40, 60, and 80%)

After the tests, the cell was fractured and its surface, cross section, and elemental distribution were characterized by scanning electronic microscope (SEM) and energy-dispersive spectrometer (EDS) using an electron probe microanalyzer (JSM-6460, JEOL, Japan). The actual thickness of the cell components was also determined using SEM together with EDS. The porosity and tortuosity of the porous anode layer before and after the cell tests were determined using mercury porosimetry (AutoPore IV 9510, Micromeritics, USA) and image analysis.[9]

EIS Spectra Simulation

General approach.— For an isothermal electrochemical system, the general approach for electrochemical impedance spectra simulation is shown in Fig. 2. The approach is based on combining transient modeling, EIS simulation, parameter estimation, and experimental validation. Because it is the most common in EIS measurements, the voltage perturbation was considered sinusoidal. Note that the charge balance, mass balance, energy balance, and momentum balance can be incorporated into the transient physicochemical model. However, because the EIS measurements were carried out in this paper in an SOFC button cell, only the charge and mass balances were considered here. Once the transient model was solved, its results were converted into EIS spectra, which were then compared to the EIS spectra obtained experimentally. The model was first calibrated for a given set of experimental conditions by varying some model parameters, as described in the model calibration section. Once calibrated, the model was then validated for a wider range of operating conditions, and finally sensitivity analysis was performed to better understand the influence of the parameters that were tuned during the calibration step and to isolate those that would need particular attention.

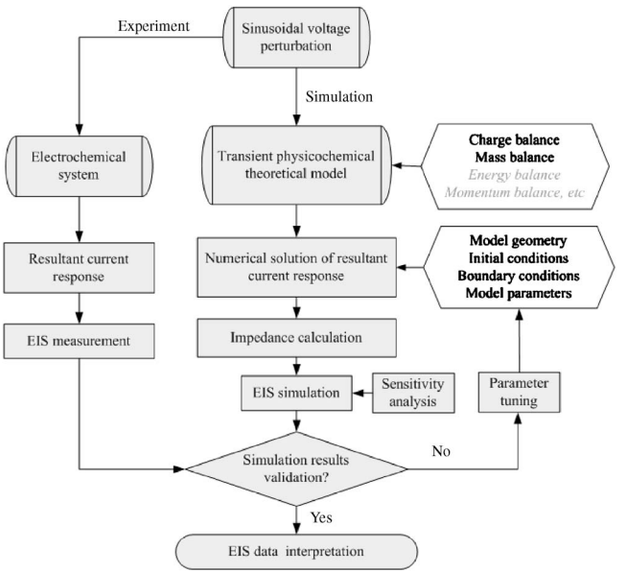

Figure 2. Simulation approach of EIS.

Transient SOFC positive-electrolyte-negative structure (PEN) model formulation.— Model assumptions and model geometry.— The model is based on physical conservation laws and can be solved in different dimensions. In order to simplify the calculation, the physicochemical model is derived in a one-dimensional (1D) computing domain as shown in Fig. 3 to represent a button cell. The reactant gas mixtures are approximated as ideal gases, thus gas-mixture physical properties such as specific viscosity, density, etc., can be easily estimated for any mixed-gas compositions. The reaction active sites are assumed to be uniformly distributed in the electrode, and the two conducting phases, electronic and ionic, were considered to be continuous and homogeneous. Because the reaction zone may spread into the anode support layer, especially if the active layer is relatively thin, the governing equations for the anode-supported layer were the same as that of the anode active layer. The temperature is considered uniform throughout the cell; thus, the model is assumed to be isothermal. The convection flux is negligible in the porous electrode compared to species diffusion, and thus pressure gradient within the porous electrode is neglected.

With the above assumptions and model geometry, an SOFC transient model is formulated using charge balance and mass balance together with electrochemical reaction kinetics as described in the following sections.

Governing equations.— Most of the steady-state forms of the governing equations have been presented in detail in previous papers.[14,16,17] Here, only the transient forms of the governing equations are presented.

For the electrodes, the effects of double-layer capacitance should be considered, and the charge-balance equations are formulated as

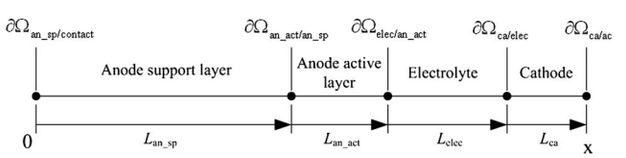

Figure 3. Illustration of simplified 1D model geometry of SOFC button cell.

$$\frac{\partial[C_{dl}S_{act}(V_i - V_j)]}{\partial t} + \nabla(-\sigma^{eff}\nabla V_i) = Q \quad [1]$$

where t is time, C_{dl} is the specific interface double-layer capacitance between electronic and ionic conductor phases, Q is the transfer current source, V_i and V_j denote the electric potential of the two conductor phases, σ^{eff} is the effective electronic or ionic conductivity, and S_{act} is the active surface area per unit volume defined as the contact area of different types of particles. This parameter has been formulated by some researchers using the particle coordination number in binary random packing of spheres, together with percolation theory given as[16,18,19]

$$S_{act} = \pi \sin^2\theta r_{el}^2 n_t n_{el} n_{io} Z_{el} Z_{io} P_{el} P_{io}/Z \quad [2]$$

where r_{el} is the mean radius of the electronic conductor particle, θ is the contact angle between two different particles and is set as 15° in this paper, n_t is the total number of particles per unit volume, n_{el} and n_{io} are the fraction number of electronic conductor and ionic conductor particles, respectively, Z_{el} and Z_{io} are the coordination numbers of electron and ion conductor particles, and P_{el} and P_{io} are the whole range connection probabilities of the same kind particles. The model formulation and the methods to calculate the parameters can be found in the literature.[18,19] In this paper, the calculated value of S_{act} in the anode support layer, active layer, and cathode layer are 6.55, 9.83, and 6.55×10^4 m^2 m^{-3}, respectively.

The governing equations for the electrode charge balances are summarized as follows.

Ionic charge at the cathode

$$\frac{\partial[C_{dl,ca}S_{act,ca}(V_{ion,ca} - V_{elec,ca})]}{\partial t} - \nabla(\sigma_{ion,ca}^{eff}\nabla V_{ion,ca}) = Q_{ion,ca}$$
$$= -i_{0,ca}S_{act,ca}\left\{\frac{c_{O_2}^{TPB}}{c_{O_2}^{bulk}}\exp\left[\frac{\alpha n_e F(V_{elec,ca} - V_{ion,ca} - V_{ref,ca})}{RT}\right] - \exp\left[-\frac{(1-\alpha)n_e F(V_{elec,ca} - V_{ion,ca} - V_{ref,ca})}{RT}\right]\right\} \quad [3]$$

Electronic charge at the cathode

$$\frac{\partial[C_{dl,ca}S_{act,ca}(V_{elec,ca} - V_{ion,ca})]}{\partial t} + \nabla(-\sigma_{elec,ca}^{eff}\nabla V_{elec,ca}) = Q_{elec,ca} = -Q_{ion,ca} \quad [4]$$

Ionic charge at the anode

$$\frac{\partial[C_{dl,an}S_{act,an}(V_{ion,an} - V_{elec,an})]}{\partial t} - \nabla(\sigma_{ion,an}^{eff}\nabla V_{ion,an}) = Q_{ion,an}$$
$$= i_{0,an}S_{act,an}\left\{\frac{c_{H_2}^{TPB}}{c_{H_2}^{bulk}}\exp\left[\frac{\alpha n_e F(V_{elec,an} - V_{ion,an} - V_{ref,an})}{RT}\right] - \frac{c_{H_2O}^{TPB}}{c_{H_2O}^{bulk}}\exp\left[-\frac{(1-\alpha)n_e F(V_{elec,an} - V_{ion,an} - V_{ref,an})}{RT}\right]\right\} \quad [5]$$

Electronic charge at the anode

$$\frac{\partial[C_{dl,an}S_{act,an}(V_{elec,an} - V_{ion,an})]}{\partial t} + \nabla(-\sigma_{elec,an}\nabla V_{elec,an}) = Q_{elec,an} = -Q_{ion,an} \quad [6]$$

The expression for the anode exchange current density (both anode support layer and anode active layer) is formulated as

$$i_{0,an} = \frac{\beta_{an}RT}{3F}\left(\frac{c_{H_2}}{c_{ref,H_2}}\right)\exp\left(-\frac{E_{act,an}}{RT}\right)(p_{O_2,an})^{0.133} \quad [7]$$

where $i_{0,an}$ is the anodic exchange current density, c_{ref,H_2} is the hydrogen concentration in the reference case, and $p_{O_2,an}$ is the oxygen

partial pressure at the anode. For the support layer we kept the values found in Nagata et al.,[20] that is, $E_{act,an} = 120{,}000$ J mol^{-1} and $\beta_{an} = 6.17 \times 10^{11}\ \Omega^{-1}\ m^{-2}$. For the active layer, $E_{act,an}$ is kept constant at 120,000 J mol^{-1} and β_{an} is treated as an adjustable parameter to fit the experimental data. The $p_{O_2,an}$ is the oxygen partial pressure at the anode assumed at equilibrium with H_2 and H_2O and is thus calculated as

$$p_{O_2,an} = \left(\frac{p_{H_2O}}{K_{eq,H_2} p_{H_2}} \right)^2 \quad [8]$$

where K_{eq,H_2} is the equilibrium constant of hydrogen oxidation reaction.

The cathode exchange current density is expressed as the expression found in Costamagna et al.[18]

$$i_{0,ca} = \frac{\beta_{ca} RT}{4F} \exp\left(- \frac{E_{act,ca}}{RT} \right) (p_{O_2,ca})^{0.25} \quad [9]$$

where $i_{o,ca}$ is the cathode exchange current density and $p_{O_2,ca}$ is the oxygen partial pressure at the cathode. $E_{act,ca}$ is kept constant at 130,000 J/mol while β_{ca} is also treated as an adjustable parameter, similar to β_{an}.

For the electrolyte layer, there are no current sources or sinks. Consequently, the electrolyte charge balance equation is written as

$$\nabla(- \sigma^{eff}_{ion,electrolyte} \nabla V_{ion}) = 0 \quad [10]$$

where $\sigma^{eff}_{electrolyte}$ is the effective ionic conductivity of the electrolyte and V_{ion} is the local ionic potential.

V_{ref} is the local relative potential difference between the electronic and ionic conductors at a reference state. By setting $V_{ref,an}$ to zero, the cathode reference potential $V_{ref,ca}$ becomes the local open-circuit voltage and can be formulated as

$$\begin{aligned} V_{ref,ca} &= V_{op} + V_{ref,an=0} = V_{op,th} - \eta_{leak} \\ &= E^0 - \frac{RT}{2F} \ln\left(\frac{p^{0.5}_{O_2,ca} p_{H_2,an}}{p_{H_2O,an}} \right) - \eta_{leak} \end{aligned} \quad [11]$$

where V_{op} denotes the actual cell open-circuit voltage, $V_{op,th}$ is the theoretical open-circuit voltage, E^0 is the standard cell potential, and $p_{H_2,an}$ and $p_{H_2O,an}$ are the partial pressures of hydrogen and water at the anode, respectively. η_{leak} is the leak overpotential, kept constant here at 0.03 V.

The mass balance in porous electrode can be formulated as

$$\frac{\partial(\varepsilon \rho w_i)}{\partial t} + \nabla (J_i) = R_i \quad [12]$$

where ε is the porosity, ρ is the density of the gas mixture, and w_i is the mass fraction of species *i*. J_i denotes the mass diffusion flux of species *i*. R_i is the reaction rate of species *i*, which could be formulated as

$$J_i = M_i N_i \quad [13]$$

where M_i is the molecular weight of species *i*. N_i is the mole diffusion flux of species *i*.

It is generally agreed that one of the most convenient approaches for modeling the combined free molecular diffusion and Knudsen diffusion flux is the dusty-gas model, which is a modified form of the Maxwell–Stefan diffusion equations.

The dusty-gas model was formulated as follows while neglecting the pressure gradient in the porous electrode,[21] and the implicit relationship between the species mole fraction and molar diffusion fluxes was provided

$$- c \nabla x_i = \sum_{j=1, i \neq j}^{n} \left(\frac{x_j N_i - x_i N_j}{D^{eff}_{ij}} \right) + \frac{N_i}{D^{eff}_{kn,i}}, \quad i = 1,2,3 \ldots, n \quad [14]$$

where the effective molecular diffusion coefficients D^{eff}_{ij} and the effective Knudsen diffusion coefficients $D^{eff}_{kn,i}$ can be calculated by considering the porous material property as[22]

$$D^{eff}_{ij} = \frac{\varepsilon}{\tau} D_{ij} = \frac{0.00101 T^{1.75} \left(\frac{1}{M_i} + \frac{1}{M_j} \right)^{1/2}}{P[V_i^{1/3} + V_j^{1/3}]^2} \quad [15]$$

$$D^{eff}_{kn,i} = \frac{\varepsilon}{\tau} D_{kn,i} = 97.0 \frac{\varepsilon \bar{r}}{\tau} \sqrt{\frac{T}{M_i}} \quad [16]$$

where ε denotes the electrode porosity and τ denotes the tortuosity factor. *V* is the diffusion volume, and $\bar{r}$ denotes the average pore radius.

Equation 14 can be formulated as the explicit relationship between species model fractions and molar fluxes using matrix notation[23]

$$(N_i) = - c[B]^{-1}(\nabla x_i) = - c[\tilde{D}](\nabla x_i) = \left(- c \sum_{j=1}^{n} \tilde{D}_{ij} \nabla x_j \right) \quad [17]$$

where the elements of square matrix [B] can be formulated as

$$B_{ij} = \begin{cases} \dfrac{1}{D^{eff}_{kn,i}} + \displaystyle\sum_{k=1}^{n} \frac{x_k}{D^{eff}_{ik}}, & j = i \\ - \dfrac{x_i}{D^{eff}_{ij}}, & j \neq i \end{cases} \qquad i,j = 1,2,3 \ldots, n \quad [18]$$

The $[\tilde{D}]$ is the inverse of the matrix [*B*], and the elements of $[\tilde{D}]$ can be treated as the effective multicomponent diffusivity according to the dimension of its unit.

Then, by substituting Eq. 17 into Eq. 12, we can get

$$\begin{aligned} &\frac{\partial(\varepsilon \rho w_i)}{\partial t} + \nabla \left(- c M_i \sum_{j=1}^{n} \tilde{D}_{ij} \nabla x_j \right) \\ &= \frac{\partial(\varepsilon \rho w_i)}{\partial t} + \nabla \left(- \rho w_i \sum_{j=1}^{n} \tilde{D}_{ij} \nabla x_j \right) = R_i \end{aligned} \quad [19]$$

The equations for electrode mass balances can be summarized as follows:

Mass balance at the anode

$$\frac{\partial(\varepsilon_{an} \rho_{an} w_{H_2})}{\partial t} + \nabla \left(- \rho w_{H_2} \sum_{j=1}^{n} (\tilde{D}_{H_2,j} \nabla x_j) \right) = \frac{- i_{trans,an} S_{act,an} M_{H_2}}{2F} \quad [20]$$

$$\begin{aligned} &\frac{\partial(\varepsilon_{an} \rho_{an} w_{H_2O})}{\partial t} + \nabla \left(- \rho w_{H_2O} \sum_{j=1}^{n} (\tilde{D}_{H_2O,j} \nabla x_j) \right) \\ &= \frac{- i_{trans,an} S_{act,an} M_{H_2O}}{2F} \end{aligned} \quad [21]$$

For binary H_2/H_2O systems, Eq. 21 is not needed and the water concentration is simply found from the hydrogen mass fraction. For ternary ($H_2/H_2O/N_2$) systems, Eq. 21 must be solved. The nitrogen concentration is then determined from the mass fraction of all components (see Eq. 22)

Table I. Boundary conditions.

	Ionic charge	Electronic charge	Mass balance
$\partial\Omega_{ca/cc}$	Insulation	$V_{cell,ca}$	$w_{O_2,ca,bulk}$, $w_{N_2,ca,bulk}$ [a]
$\partial\Omega_{ca/elec}$	Continuity	Insulation	Insulation
$\partial\Omega_{elec/an\_act}$	Continuity	Insulation	Insulation
$\partial\Omega_{an\_act/an\_sp}$	Continuity	Continuity	Continuity
$\partial\Omega_{an\_sp/ac}$	Insulation	$V_{cell,an}$	$w_{H_2,an,bulk}$, $w_{H_2O,an,bulk}$, $w_{N_2,an,bulk}$ [a]

[a] $w_{i,bulk}$ are the mass fractions of species i in the fuel or air channel.

$$\sum_i w_i = 1 \qquad [22]$$

Mass balance at the cathode

$$\frac{\partial(\varepsilon_{ca}\rho_{ca}w_{O_2})}{\partial t} + \nabla\left(-\rho w_{O_2}\sum_{j=1}^{n}(\tilde{D}_{O_2,j}\nabla x_{O_2})\right) = \frac{i_{trans,ca}S_{act,ca}M_{O_2}}{4F} \qquad [23]$$

The nitrogen concentration in cathode is also determined from the mass fraction of all components (see Eq. 22).

Boundary conditions.— In order to solve the system of coupled partial-differential equations of charge and mass balances in the time domain, the boundary conditions are specified in Table I.

The boundary condition "insulation" means that the partial derivative of the variable at the boundary is zero and there is no flux through the boundary. Note that the difference between $V_{cell,ca}$ and $V_{cell,an}$ is the cell voltage used in the calculation. Here, we chose $V_{cell,an} = 0$. $V_{cell,ca}$ can be divided into a stationary part, V_{st}, and a transient part, $V_p \sin(\omega t)$, as shown in following equation

$$V_{cell,ca} = V_{st} + V_p \sin(\omega t) \qquad [24]$$

The stationary part denotes the bias voltage used in the EIS measurements, and the transient part denotes the sinusoidal perturbation in voltage in which ω and V_p are the angle frequency and amplitude of perturbation signals, respectively.

Transient symmetric cathode cell model.— To solve the model for the full button cell, six parameters need to be tuned, three for the anode (β_{an}, τ_{an}, and $C_{dl,an}$) and three for the cathode (β_{ca}, τ_{ca}, and $C_{dl,ca}$). Instead of fitting six parameters at once, it is possible to independently fit the three cathode parameters using a symmetric cathode cell. The preparation method and the measurement of the symmetric cathode cell have been discussed in detail in one of our previous papers.[14] Once the cathode parameters have been determined, only three parameters (the anode ones) need to be fitted using the full button cell model. For the symmetric cathode cell, the governing equations for charge and mass balances are the same as those for the cathode in the transient button cell model. The only difference is the model geometry, shown in Fig. 4.

Transient model solution and EIS spectra synthesis.— The governing partial-differential equations were computationally solved using the finite element software Comsol Multiphysics, version 3.2.

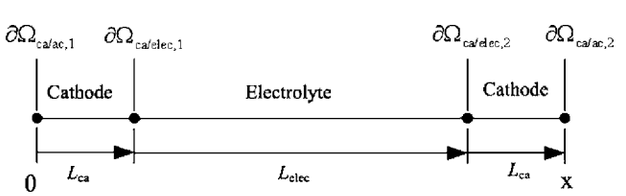

Figure 4. Model geometry for the symmetric cathode cell.

For a given set of bias voltage, perturbation amplitude, and frequency for the input voltage (see Eq. 24), the model was run for several periods just like the experimental measurements of the EIS. If the EIS measurements are carried out at the open-circuit state, $V_{cell,ca}$ represents the cell open-circuit voltage. Usually, after about 10 periods, a steady oscillating solution of current density was achieved. Because the perturbation voltage was sinusoidal, the response current density i_{cell} was also a periodic function.

For a general analytical expression, i_{cell} can be expanded into a Fourier series without considering the contribution of the numerical noise-to-current density signals as discussed in detail by Bessler[11] and Zhu and Kee,[13] as seen in Eq. 25

$$i_{cell} = i_{st} + \sum_{k=1}^{\infty} i_{p,k}\sin(k\omega t - \phi) \qquad [25]$$

where ϕ is the phase shift angle from imposed perturbation voltage to current density response, i_{st} is the stationary part of current density, and $i_{p,k}$ are the measures of the electrochemical system nonlinearities.

In this study, for both experiment and simulation, the perturbation voltage was set to a small value (10 mV) such that a linear current density response was obtained. In this case, only $i_{p,1}$ is the nonzero component of the current density transient response. By writing $i_{p,1}$ as i_p, the cell current density is formulated as

$$i_{cell} = i_{st} + i_p \sin(\omega t - \phi) \qquad [26]$$

Multiplying Eq. 26 by $\sin(\omega t)$ and $\cos(\omega t)$, then integrating over a full period τ, results in

$$i_p \cos\phi = \frac{2}{\tau}\int_0^{\tau} i_{cell}\sin(\omega t)dt \qquad [27]$$

$$i_p \sin\phi = \frac{2}{\tau}\int_0^{\tau} i_{cell}\cos(\omega t)dt \qquad [28]$$

From the two equations shown in Eq. 27 and 28, i_p and ϕ can then be determined.

Using complex notation to write the impedance response in terms of a real and an imaginary component, results in

$$Z = \frac{V_{cell}}{i_{cell}} = \frac{V_p\exp(j\omega t)}{i_p\exp(j\omega t - j\phi)} = Z_{real} + Z_{imag} = \frac{V_p}{i_p}\cos\phi + j\frac{V_p}{i_p}\sin\phi \qquad [29]$$

Finally, in order to generate Nyquist and Bode plots, the calculations must be performed over a range of frequencies to calculate the corresponding impedance, as is done for the experimental measurements. However, the frequency f used in the experimental measurements must be converted to the angle frequency according to $\omega = 2\pi f$.

For a mesh grid number equal to 76 (a number deemed sufficient to model the cell behavior correctly), time step equal to $\frac{1}{20}$ period, time span equal to 15 periods, and the number of frequency points equal to 31, the total calculation time for a whole EIS spectra is around 30 min on a small computation workstation (Intel Xeon 3.2 GHz, 4GB memory).

The simulation approach could involve charge balance, mass balance, momentum balance, and energy balance, and the transient model could be solved for different geometries and different dimensions. As a result, the proposed approach can be thought of as a comprehensive emulator to the EIS experiment, as the working principles of the simulation and the experiment are almost the same. However, this method quickly becomes computationally intensive as higher dimension models and/or addition of energy/mass balances are considered.

Table II. Material conductivities.

Parameter	Value
ScSZ conductivity (S m^{-1})	$6.92 \times 10^4 \exp(-80488/T)$[a]
YSZ conductivity (S m^{-1})	$3.34 \times 10^4 \exp(-10300/T)$[b]
LSM conductivity (S m^{-1})	$4.2 \times 10^7 \exp(-1150/T)/T$[b]
Ni conductivity (S m^{-1})	$3.27 \times 10^6 - 1065.3T$[c]
Equivalent ionic conductivity of electrolyte layer (S m^{-1})	$0.002T - 1.4483$[a]
Porosity of cathode and anode support layer and anode active layer	0.364[d]
Mean pore diameter of cathode and anode support layer (μm)	0.46[d]
Mean pore diameter of anode active layer (μm)	0.31[d]

[a] Determined experimentally.
[b] Ref. 24.
[c] Ref. 25.
[d] Ref. 14.

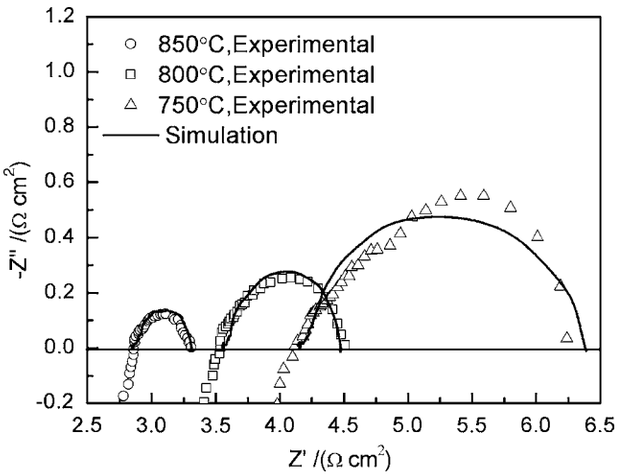

Figure 5. EIS spectra for the symmetric cell. Comparison between experimental and simulated data using tuned parameters for the cathode. H_2/H_2O (95.8/4.2%) fuel.

Results and Discussion

Model parameters.— Table II lists the conductivities of ionic and electronic conductors as well as the equivalent conductivity of the electrolyte layer (i.e., when the whole conductivity of the cell is reduced to that of the electrolyte layer), which was determined by EIS spectra at open-circuit state.

Because some parameters could not be determined directly from experiments or from published data, a tuning process was necessary for estimating these parameters, as described in the next section. This tuning, or calibration, where some parameters were allowed to vary, was performed for a limited number of experiments (calibration sets). Once determined, these parameters were not allowed to be changed when comparing the results from the simulation with those of all remaining experiments (validation set).

Model calibration.— Model calibration for cathode parameters using symmetric cell.— The symmetric-cell experiments were carried out with air at atmospheric pressure and at temperatures of 750, 800, and 850°C. The EIS spectra at all three temperatures were measured experimentally and simulated at open-circuit state with an amplitude of 10 mV over the frequency range 0.1 Hz to 100 kHz. The tuned parameters for the cathode are shown in the first column of Table III. This table also shows the value of the tuned parameters for the cathode and values reported in the literature. Using the tuned values, the EIS spectra for the symmetric cell at three temperatures are shown in Fig. 5. It was possible to obtain a good fit at 800 and 850°C, but the fit was less satisfactory at 750°C. A possible reason is a processes such as surface diffusion that is not taken into account in the model and that might become more important at lower temperatures.

Table III. Tuned parameters.

Parameters	Value	Values in literature
Cathode (using symmetric cell)		
β_{ca} in Eq. 7 (Ω^{-1} m^{-2})	6.1×10^{10}	1.05×10^{10}[a]
Cathode tortuosity	3	2.5–3[b]
$C_{dl,ca}$(F m^{-2})	27	0.05–27.4[c]
Anode (using button cell)		
β_{an} in Eq. 6 (Ω^{-1} m^{-2})	3.2×10^{12}	6.17×10^{11}[a]
Anode tortuosity	8.5	2.0–10[b]
$C_{dl,an}$(F m^{-2})	27	0.1–27.4[c]

[a] Ref. 20.
[b] Ref. 26.
[c] Ref. 13 and 27-29.

Model calibration based on button cell experimental data.— The operating conditions for the experiments used for calibrating the model are listed in Table IV. The EIS spectra at three temperatures (750, 800, and 850°C) were calculated and measured experimentally at open-circuit state with an amplitude of 10 mV over the frequency range 0.1 Hz to 100 kHz. The anode-model parameters that were tuned to match the measured EIS data for the calibration experiments are shown in Table III. Figure 6a shows that the simulated Nyquist impedance spectra agreed well with the experimental data. In the Bode impedance representations shown in Fig. 6b and c, good agreement between the simulated and experimental data was also found.

However, there still exist some deviations at both ends of the frequency range. The biggest difference occurs at high frequency where an inductive behavior, due to the lead,[3] was observed in the experiments. Because the model did not take into account any lead-related phenomena, the simulation results did not show any inductive behavior at high frequency. This is different from results we reported previously[17] that were incorrect because of a mathematical treatment that was not fully appropriate. Simulating EIS spectra involves the integration of a function dependent on current density over one period (Eq. 27 and 28). It turned out that, depending on the initial guess, the number of periods to reach a steady solution can vary greatly. In our previously reported results, this problem was overlooked. We did not start with good initial guesses and we did the integration after 10 periods, which was too short to reach a steady solution at high frequency. This issue has now been resolved, first by choosing the initial guess with more care and by making sure that a steady solution was reached. Note that good initial guesses can significantly reduce the number of required periods, the latter being also dependent on the frequency; it takes more periods to reach a steady solution as the frequency increases. Also, a small,

Table IV. Operating conditions for the calibration experiments.

Parameters	Value
Pressure, p (Pa)	101325
Temperature, T (°C)	750/800/850
Fuel composition	95.8% H_2 and 4.2% H_2O
Oxidant composition	21% O_2 and 79% N_2.

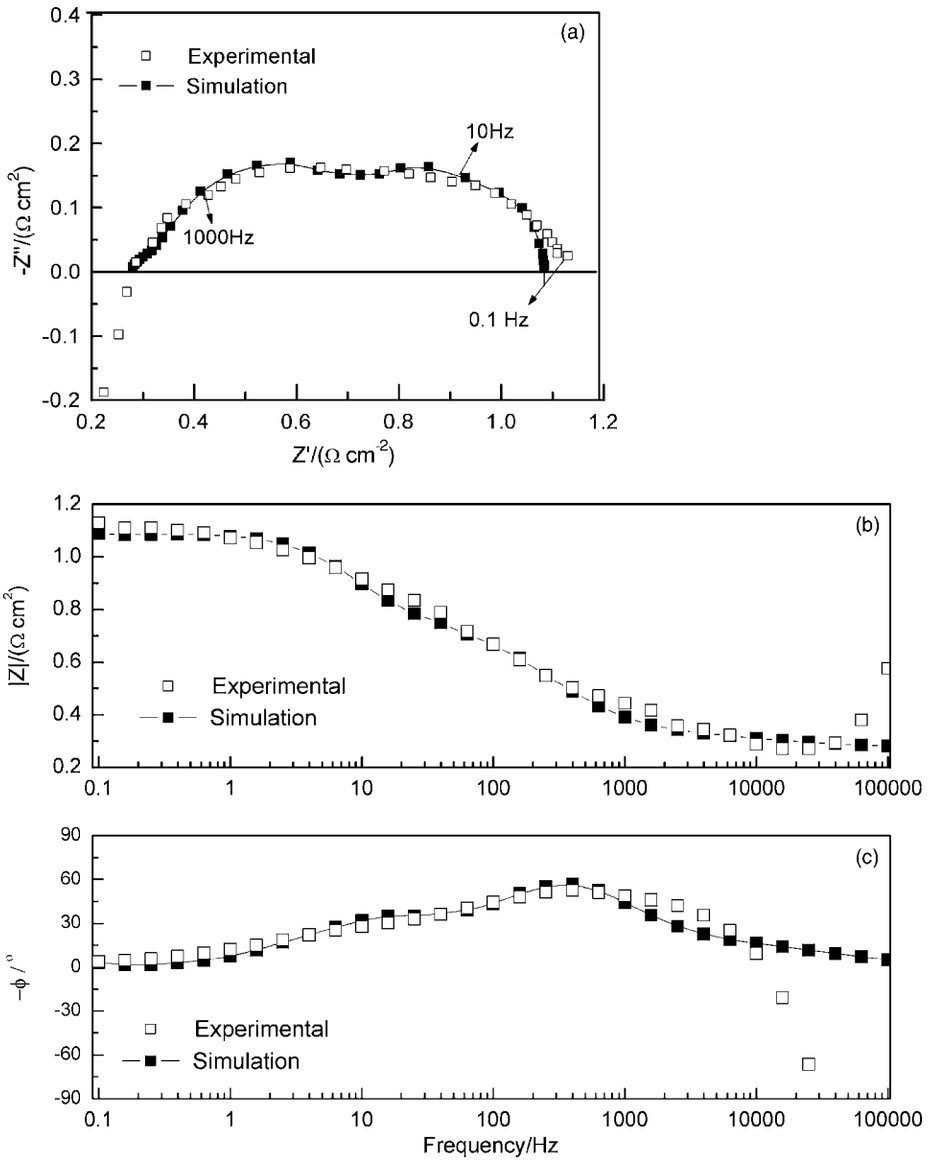

Figure 6. Experimental and simulated impedance of SOFC button cell: (a) Nyquist plot and (b) and (c) Bode plots.

low-frequency semicircle is shown in the Nyquist plot, probably due to diffusion limitation in the gas chamber as well as diffusion limitation of the nickel felt, which eventually affected the gas diffusion from the gas chamber to the anode surface. The effect of the nickel felt could eventually be indirectly deduced from Fig. 5 (symmetric cathode EIS spectra) where we did not use the porous nickel felt and for which the low-frequency semicircle was not as obvious. However, because the low-frequency semicircle is small and the experiments in this paper are more focused on the PEN itself, we have neglected the effects of diffusion limitations in the gas chamber and in the nickel felt.

Figure 7 shows the simulated and experimental EIS results at different temperatures (750, 800, and 850°C). The simulated results and experimental data agreed well for all temperatures considered here. This figure obviously shows that the cell temperature affects fuel cell resistance; as expected, both high- and low-frequency resistances increase with decreasing temperature. This is not only because lower temperatures decrease the ionic conductivity of the electrolyte, but also because they increase the reaction activation and species transport resistances.

A useful aspect of simulating EIS spectra is that it is possible to artificially isolate some phenomena, such as concentration effect on

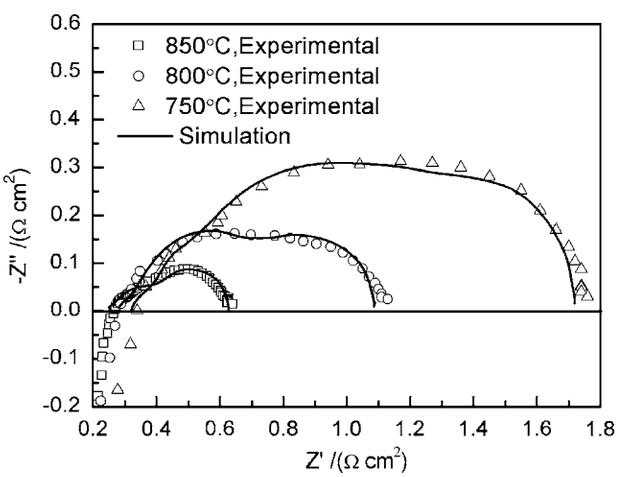

Figure 7. EIS spectra at different temperatures using H_2 fuel and air oxidant. Constant H_2O concentration of 4.2%.

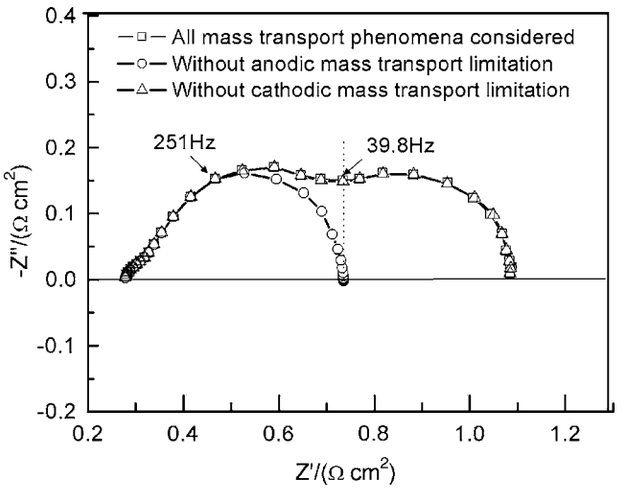

Figure 8. EIS spectra with or without anodic or cathodic mass-transport limitation. H_2/H_2O (95.8/4.2%) fuel, air oxidant, 800°C, and open-circuit voltage.

the EIS spectra. Figure 8 compares EIS spectra between the case where all phenomena are taken into consideration and cases where mass-transport limitations at the anode or cathode are eliminated. This is done by setting the source terms in the mass balances to zero (Eq. 20-22 for the anode and Eq. 22 and 23 for the cathode). Figure 8 shows that removing the source term at the cathode has no effect on the EIS spectra, which means that there is no mass-transport limitation at the cathode. This could be expected because of the thin cathode considered here. Figure 8 clearly shows the impact of mass-transport limitation on the EIS spectra, particularly at low frequencies. In this case it can be concluded that mass-transport limitation at the anode contributes to the impedance for frequencies below 251 Hz and that at frequencies below 39.8 Hz the impedance is solely due to transport limitation at the anode.

The transient model in this paper not only could be used to simulate the EIS spectra but also could be used to simulate the cell steady-state polarization curves as shown in Fig. 9. The cell steady-state performance at three temperatures (750, 800, and 850°C) were calculated and measured experimentally for the conditions shown in Table IV and parameters given in Table III. The steady-state polarization curves in Fig. 6 also show good agreement with the experimental results. The cell open-circuit voltages have been calibrated using a tuning leak overpotential parameter, whose value was found to be about 0.03 V in our experiments. The operating temperatures obviously affect the fuel cell performance, which is consistent with what was determined from the EIS spectra (see Fig. 5).

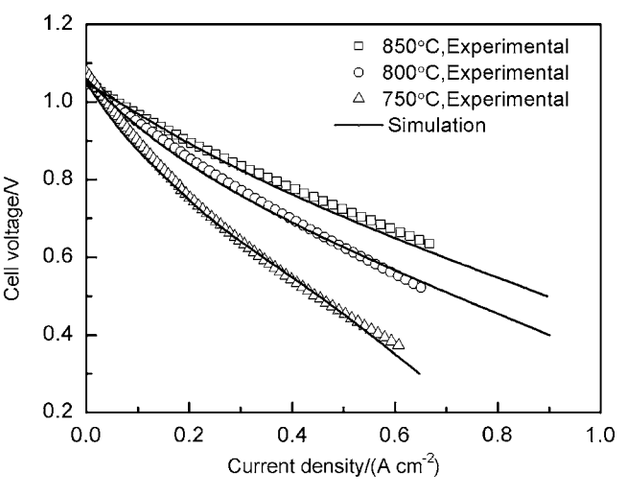

Figure 9. Polarization curves at different temperatures using H_2 fuel and air oxidant. Constant H_2O concentration of 4.2%.

Electrochemical system response.— Figure 10 gives more details on the simulated dynamic response of the SOFC electrochemical system for different perturbation voltage frequencies. The H_2 mole fraction refers to that at the anode/electrolyte layer as determined by the model. The response current density amplitude increases with increasing frequency. Because the impedance amplitude decreases with increasing frequencies (see Fig. 6b), the amplitude of the current density, which is inversely proportional to that of the impedance, increases with increasing frequencies. The larger cell impedance at lower frequencies is mainly due to the relatively larger mass-transfer resistance. The reason for this effect can be explained by examining the variation in H_2 concentration at different frequencies, as shown in Fig. 10. At higher frequencies, the H_2 concentration at the anode/electrolyte interface shows small amplitude changes and stays around its steady-state value, while at lower frequencies the amplitude of the H_2 concentration increases. At 0.1 Hz, the H_2 concentration amplitude is about 5% of its steady-state value, which leads to larger mass-transfer resistance. From the simulation results, it can also been seen that the phase angle remains around zero at 0.1 Hz, and increases for a frequency of 10 Hz. At 1000 Hz the phase angle is nearly 45° (approximately determined from the displacement of voltage curves and current density curves along the *x* axis). The above observations about phase angle at different frequencies can also be seen in Fig. 6c.

Sensitivity analysis.— It is difficult to estimate the effects of each model parameter on the model outcomes, and simulated impedance spectra, in general, do not show a simple dependence on a single parameter. Sensitivity analysis can be used to interpret these complex interdependences. Figure 11 shows the sensitivity analysis of the impedance magnitude and phase angle on the tuned parameters at three frequencies (0.1, 10, and 1000 Hz) when the tuned parameters were decreased by 10% from their original value (see Table III).

Magnitude sensitivity.— The anode tortuosity has a negligible effect on the magnitude at high frequencies because at these conditions, the impedance is weakly influenced by mass transport. However, because of the thick anode, the effect of anode tortuosity becomes apparent as the frequency decreases. A decrease in anode tortuosity facilitates mass transport, thus the decrease in impedance magnitude seen in Fig. 11a for a 10% decrease in anode tortuosity. Note that the effect of cathode tortuosity on the magnitude is negligible because the cathode is thin (15 μm), and transport limitations are thus negligible. The exchange current density is proportional to that of β shown in Fig. 11 (see Eq. 6 and 7), and thus any relative change in β is representative of changes in exchange current density. Figure 11 therefore indicates that changes in exchange current density have no apparent effect on the impedance magnitude at high frequencies, but have a noticeable influence at lower frequencies, especially for the cathode exchange current density. Also, reducing the exchange current density increases the impedance magnitude. At the lowest frequency (0.1 Hz) the double-layer capacitance of both anode and cathode has no effect on the magnitude. At the cathode, C_{dl} shows some effect on the magnitude only at high frequencies. At the anode, there appears to be an intermediate frequency at which the anode double-layer capacitance has more effect on the magnitude.

Phase-angle sensitivity.— At low frequency (0.1 Hz), the phase angle is insensitive to any of the tune parameters. At 10 Hz, changes in β_{an}, τ_{ca}, and C_{dl} have little to no effect on the phase angle. At this frequency only changes of β_{ca} and τ_{an} significantly affect the phase angle. Note that at 10 Hz a decrease in both β_{ca} and τ_{an} results in a decrease in phase angle, while at 1000 Hz a decrease in any of the tuned parameters results in an increase in phase angle. At high fre-

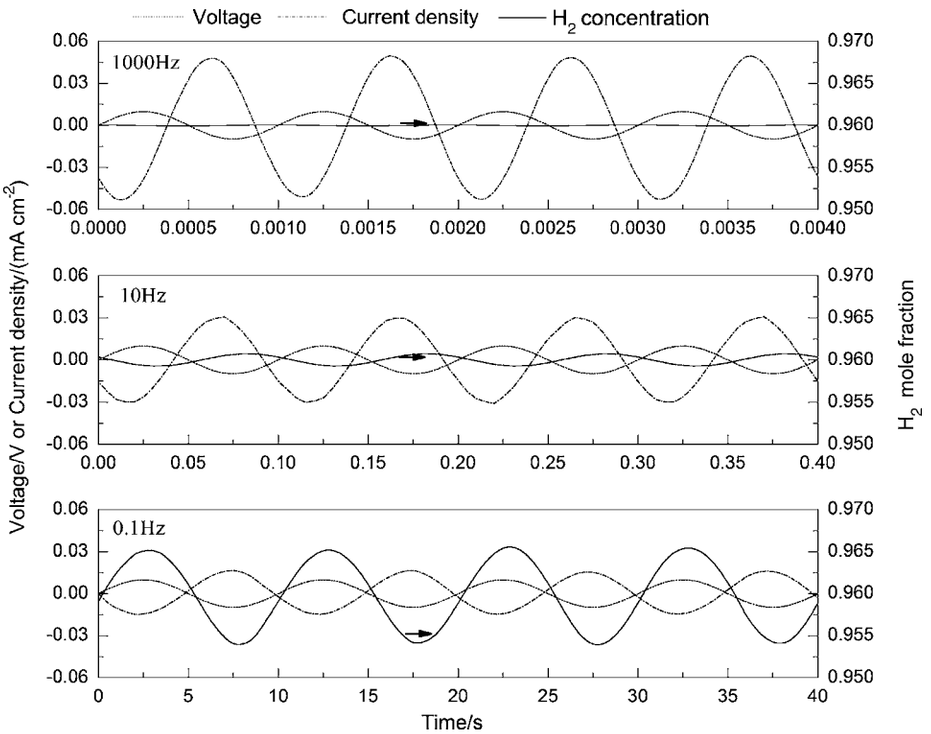

Figure 10. Transient numerical simulation of the dynamics of SOFC electrochemical system for different voltage-frequency perturbations using H_2 fuel and air oxidant at 800°C. Constant H_2O concentration of 4.2%.

quencies, the tortuosities have little impact on the phase angle. Figure. 11b also shows that at 1000 Hz, changes in cathode-related tuned parameters have more effect on the phase angle than anode-related parameters.

Model validation and discussion for extended operating conditions.— Effect of oxidant composition.— The cell polarization resistance can be effectively reduced by using pure oxygen as oxidant instead of air. Figure 12 illustrates the modeling and experimental EIS spectra at different temperatures when pure O_2 is used as oxidant. For comparison, the experimental EIS spectra for air as oxidant at 800°C is also depicted in Fig. 12. It can be observed from Fig. 12 that the modeling results agree well with the experimental data at 850 and 800°C but somewhat underestimate the cell polarization resistance at 750°C, especially at lower frequencies. The cell polarization at 800°C is lower with pure O_2 than with air. Because the cathode layer is thin (15 μm), the cathode polarization resistance is primarily dominated by activation processes rather than diffusion processes.

Effect of fuel composition (mixtures of $H_2/H_2O/N_2$).— Figure 13 shows the experimental and simulated EIS spectra for various mixtures of $H_2/H_2O/N_2$ at 800 and 850°C. In all cases, the water content was kept constant at 4.2%. Experiments with large amounts of N_2 in the fuel are only carried out for model validation in this study, because such conditions are not encountered in actual SOFC operation. The simulated EIS spectra agreed well with the experimental spectra for most concentrations at both 850 and 800°C, except toward the lower frequencies. However, discrepancies are more notable for the lowest H_2 concentration.

In general, for a given temperature, the polarization resistance decreases as the bulk partial pressure of hydrogen increases. This trend agrees well with what is observed in Fig. 13 for both simulated and experimental results. It is also clear from Fig. 13 that the lower-frequency impedances increase as the H_2 content decreases, especially at 800°C, and that the higher-frequency impedances vary little with different H_2 content. The main difference between the EIS spectra at various H_2 concentrations should be primarily related to increasing transport limitation as the H_2 concentration decreases.

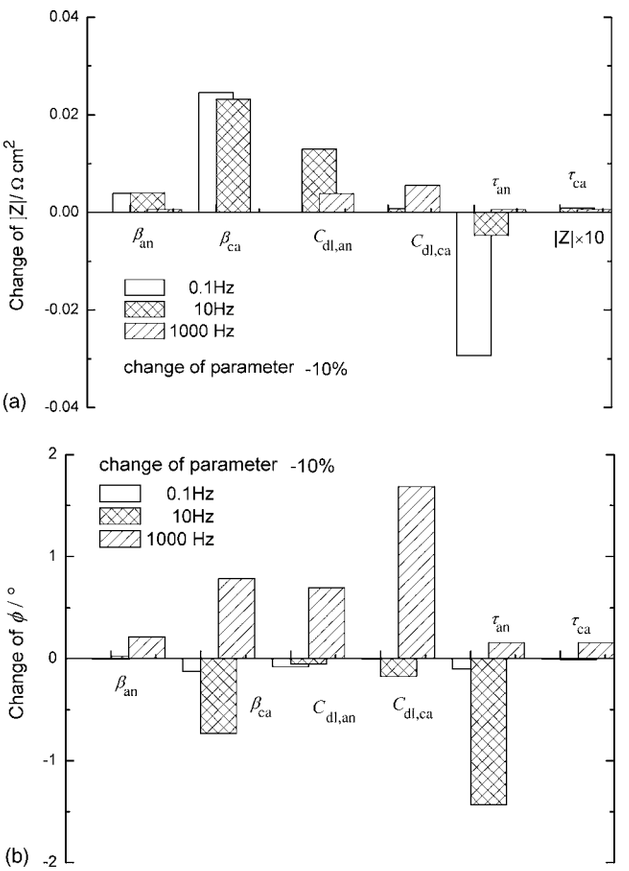

Figure 11. Sensitivity analysis for (a) magnitude and (b) phase angle on the tuned model parameters using H_2 fuel and air oxidant at 800°C. Constant H_2O concentration of 4.2%.

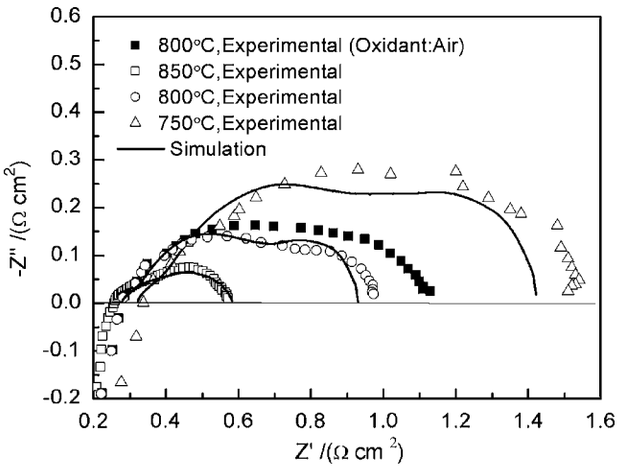

Figure 12. Simulated and experimental EIS spectra using O_2 as oxidant at 750, 800, and 850°C. Constant H_2O concentration of 4.2%.

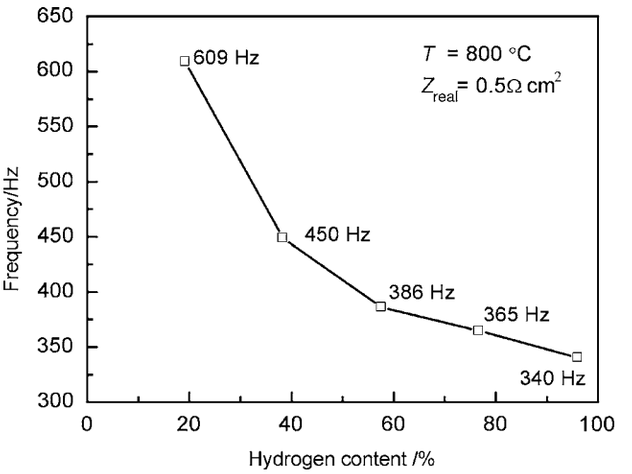

Figure 14. Frequency corresponding to 0.5 Ω cm^2 (curves start to diverge) as a function of hydrogen concentration at 800°C. Constant H_2O concentration of 4.2%.

Therefore, the portion of the curves where the lines diverge from each other should be representative of transport limitation. This is consistent with the discussion about Fig. 8, which must be compared to Fig. 13a (same operating temperature). In Fig. 8 it was deduced that mass-transport limitation at the anode begins to contribute to the impedance for a real part of the impedance above around 0.5 Ω cm^2. Figure 13a shows that this value of 0.5 also corresponds to the real part of the impedance at which the curves start diverging. Note, however, that the frequency corresponding to 0.5 Ω cm^2 varies with hydrogen concentration; the lower the hydrogen concentration; the higher the corresponding frequency at 0.5 Ω cm^2, as seen in Fig. 14. In other words, the points on the EIS spectra are moving clockwise as the concentration of hydrogen decreases. This is explained by the fact that at low frequencies, the contribution of transport phenomena to the impedance dominates. As the hydrogen concentration decreases, transport limitation becomes more and more important and, therefore, transport contribution to the impedance is seen at higher frequencies.

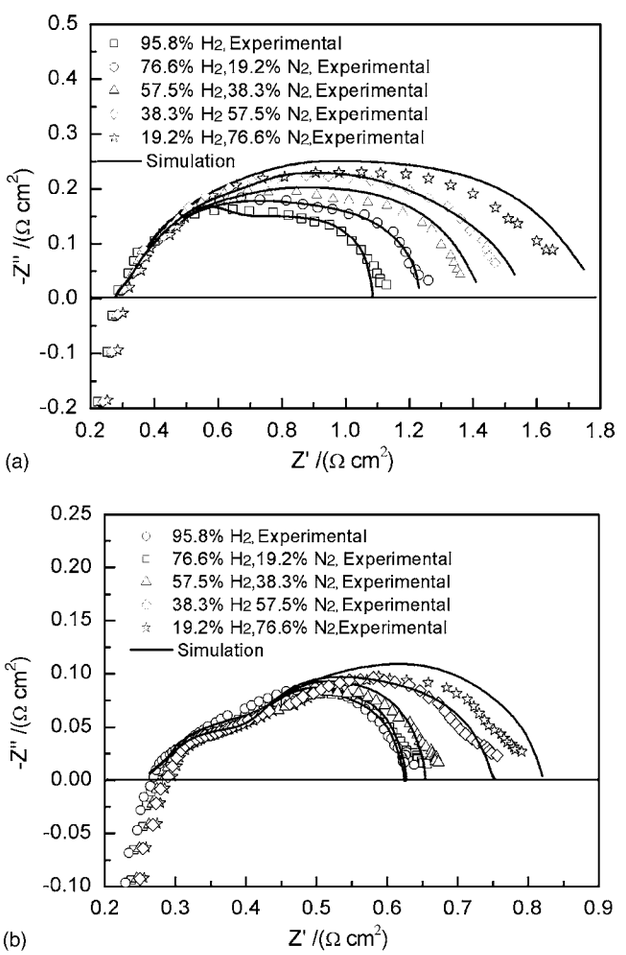

Figure 13. Simulated and experimental EIS spectra for various $H_2/H_2O/N_2$ fuel mixtures at (a) 800 and (b) 850°C. Constant H_2O concentration of 4.2%.

Conclusions

A general approach for EIS by solving in the time domain a comprehensive coupled transient model based on physical conservation laws was applied. The transient SOFC model was calibrated and validated in the case of humidified water at temperatures between 750 and 850°C using experimental EIS spectra, yielding good agreement between simulated and experimental results. In total, six parameters had to be tuned (β, τ, and C_{dl} at the cathode and at the anode). The cathode parameters were tuned independently using the data from a symmetric cathode cell. The remaining anode parameters were then tuned using the data from a button cell. The model was further validated experimentally for extended operating conditions by changing oxidant and anode feed gas composition. The validation results showed that the simulated EIS spectra agreed well with the experimental results for a wide range of operating conditions. Closer examination of the dynamic response revealed that the amplitude of hydrogen concentration at the anode/electrolyte interface increased at lower frequencies, explaining the increasing mass-transfer resistance observed at low frequencies. Simulating EIS spectra can be useful in interpreting the data. For example, it was possible to isolate the frequency range where mass transport was dominant; it was observed that the frequency range over which mass-transport limitation dominates increases as the hydrogen concentration decreases. Finally, sensitivity analysis of the impedance (magnitude and phase angle) on the tuned parameters was performed at three frequencies (0.1, 10, and 1000 Hz).

The proposed approach can represent a valuable tool to interpret EIS spectra and to build a direct relationship between two of the most import experimental techniques in electrochemical characterization: steady-state polarization curves and EIS spectra.

Tsinghua University assisted in meeting the publication costs of this article.

List of Symbols

C	concentration, mol m^{-3}
C	specific double-layer capacitance, F m^{-2}
D	diffusion coefficient, m^2 s^{-1}
E	activation energy, J mol^{-1}
F	frequency, Hz
i	current density, A m^{-2}
i_0	exchange current density, A m^{-2}
M_i	molecular weight of species i, kg/mol
P	pressure, Pa
Q	source term of charge-balance equations, A m^{-3}
R	gas constant, 8.314 J mol^{-1} K^{-1}
R_i	source term of mass-balance equations, kg m^{-3} s^{-1}
S_{act}	active surface area per unit volume, m^2 m^{-3}
t	time, s
T	temperature, K
V	electric potential or cell voltage, V
V_i, V_j	diffusion volume
w_i	mass fraction of species i

Greek letters

α	transfer coefficient
β	tuning parameter, Ω^{-1} m^{-2}
ε	porosity
η	overpotential, V
ρ	density, kg m^{-3}
σ	conductivity, S m^{-1}
τ	tortuosity
ω	angle frequency, rad s^{-1}

Superscripts

eff	effective

Subscripts

ac	anode chamber
act	activation/active
an	anode
avg	average
bulk	bulk phase
ca	cathode
cc	cathode chamber
elec	electronic
inter	interface
ion	ionic
kn	Knudsen
sp	support

References

1. N. Q. Minh and T. Takahashi, *Science and Technology of Ceramic Fuel Cells*, Elsevier Science, Amsterdam, Netherlands (1995).
2. S. C. Singhal and K. Kendall, *High Temperature Solid Oxide Fuel Cells: Fundamentals, Design and Applications*, Elsevier Advanced Technology, Oxford, U.K. (2003).
3. J. R. Macdonald and E. Barsoukov, *Impedance Spectroscopy: Theory, Experiment, and Applications*, 2nd ed., John Wiley & Sons, Hoboken, New Jersey (2005).
4. R. P. Ohayre, S.-W. Cha, W. Colella, and F. B. Prinz, *Fuel Cell Fundamentals*, John Wiley & Sons, Hoboken, New Jersey (2006).
5. A. Bieberle and L. J. Gauckler, *Solid State Ionics*, **146**, 23 (2002).
6. J. R. Wilson, D. T. Schwartz, and S. B. Adler, *Electrochim. Acta*, **51**, 1389 (2006).
7. A. Mitterdorfer and L. J. Gauckler, *Solid State Ionics*, **117**, 187 (1999).
8. A. Mitterdorfer and L. J. Gauckler, *Solid State Ionics*, **117**, 203 (1999).
9. A. Mitterdorfer and L. J. Gauckler, *Solid State Ionics*, **120**, 211 (1999).
10. W. G. Bessler, *Solid State Ionics*, **176**, 997 (2005).
11. W. G. Bessler, *J. Electrochem. Soc.*, **153**, A1492 (2006).
12. S. Gewies, W. G. Bessler, V. Sonn, and E. Ivers-Tiffee, *ECS Trans.*, **7**(1), 1573 (2007).
13. H. Zhu and R. J. Kee, *J. Electrochem. Soc.*, **153**, A1765 (2006).
14. Y. Shi, N. Cai, C. Li, C. Bao, E. Croiset, J. Qian, Q. Hu, and S. Wang, *J. Power Sources*, **172**, 235 (2007).
15. Y. Shi, N. Cai, C. Li, C. Bao, E. Croiset, J. Qian, Q. Hu, and S. Wang, *J. Power Sources*, **172**, 246 (2007).
16. Y. Shi, N. Cai, and C. Li, *J. Power Sources*, **164**, 639 (2007).
17. Y. Shi, N. Cai, C. Li, C. Bao, E. Croiset, J. Qian, Q. Hu, and S. Wang, *ECS Trans.*, **7**(1), 1889 (2007).
18. P. Costamagna, P. Costa, and V. Antonucci, *Electrochim. Acta*, **43**, 375 (1998).
19. S. H. Chan and Z. T. Xia, *Electrochim. Acta*, **148**, A388 (2001).
20. S. Nagata, A. Momma, T. Kato, and Y. Kasuga, *J. Power Sources*, **101**, 60 (2001).
21. R. Krishina and J. A. Wesselingh, *Chem. Eng. Sci.*, **52**, 861 (1997).
22. B. Todd and J. B. Young, *J. Power Sources*, **110**, 186 (2002).
23. R. Taylor and R. Krishna, *Multicomponent Mass Transfer, Wiley Series in Chemical Engineering*, Wiley, New York (1993).
24. R. J. Braun, Ph.D. Thesis, University of Wisconsin, Madison, WI, (2002).
25. J. H. Nam and D. H. Jeon, *Electrochim. Acta*, **51**, 3446 (2006).
26. S. H. Chan, X. J. Chen, and K. A. Khor, *J. Electrochem. Soc.*, **151**, A164 (2004).
27. A. M. Svesson and K. Nisancioglu, *Solid State Ionics*, **177**, 1955 (2006).
28. R. Pormprasertsuk, J. Cheng, H. Huang, and F. B. Prinz, *Solid State Ionics*, **178**, 195 (2007).
29. R. E. Williford, L. A. Chick, G. D. Maupin, S. P. Simner, and J. W. Stevenson, *J. Electrochem. Soc.*, **150**, A1067 (2003).